

Generative quantum machine learning via denoising diffusion probabilistic models

Bingzhi Zhang,^{1,2} Peng Xu,³ Xiaohui Chen,^{4,*} and Quntao Zhuang^{2,1,†}

¹Department of Physics and Astronomy, University of Southern California, Los Angeles, California 90089, USA

²Ming Hsieh Department of Electrical and Computer Engineering,
University of Southern California, Los Angeles, California 90089, USA

³Department of Statistics, University of Illinois at Urbana-Champaign, Champaign, IL 61820, USA

⁴Department of Mathematics, University of Southern California, Los Angeles, California 90089, USA

Deep generative models are key-enabling technology to computer vision, text generation and large language models. Denoising diffusion probabilistic models (DDPMs) have recently gained much attention due to their ability to generate diverse and high-quality samples in many computer vision tasks, as well as to incorporate flexible model architectures and relatively simple training scheme. Quantum generative models, empowered by entanglement and superposition, have brought new insight to learning classical and quantum data. Inspired by the classical counterpart, we propose the *quantum denoising diffusion probabilistic models* (QuDDPM) to enable efficiently trainable generative learning of quantum data. QuDDPM adopts sufficient layers of circuits to guarantee expressivity, while introduces multiple intermediate training tasks as interpolation between the target distribution and noise to avoid barren plateau and guarantee efficient training. We provide bounds on the learning error and demonstrate QuDDPM's capability in learning correlated quantum noise model, quantum many-body phases and topological structure of quantum data. The results provide a paradigm for versatile and efficient quantum generative learning.

Quantum machine learning is an emergent area in the intersection between artificial intelligence and quantum information science. Besides algorithms that require fault-tolerant quantum computers [1–3], variational parameterized quantum circuits (PQC) applicable to near-term quantum devices are proposed to complete versatile tasks [4], in analogue to classical neural networks [5–7]. In terms of generative models, quantum machine learning has brought advantage in Bayesian network [8], variational autoencoder [9], Boltzmann machine [10] and general graph models [11]. In analogy to classical generative adversarial networks (GAN) [12], quantum generative adversarial networks (QuGANs) is proposed [13–15] to process both quantum and classical data [16, 17].

Despite the success, classical GAN models are known for training issues such as mode collapse, i.e., unstable training and less diversity in generated data. In classical deep learning, denoising diffusion probabilistic models (DDPMs) and their close relatives [18–22] have recently gained much attention due to their ability to generate diverse and high-quality samples in many computer vision tasks [23–26] over the best GANs, as well as to incorporate flexible model architectures and relatively simple training scheme without adversarial training. Specifically, forward diffusion process first gradually converts the observed data to a simple random noise based on non-equilibrium thermodynamics, and then an associated time-reversal process is learned to generate samples with target distribution from the noise [18–21].

In this work, we propose the *quantum denoising diffusion probabilistic models* (QuDDPM) as an efficiently trainable scheme to generative quantum learning,

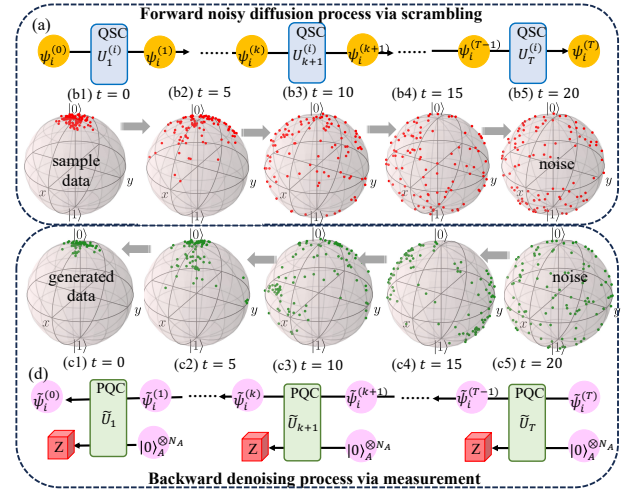


Figure 1. Schematic of QuDDPM. The forward noisy process is implemented by quantum scrambling circuit (QSC) in (a), while in the backward denoising process is achieved via measurement enabled by ancilla and PQC in (d). Subplots (b1)-(b5) and (c1-c4) presents the Bloch sphere dynamics in generation of states clustering around $|0\rangle$.

through a coordination between a forward noisy diffusion process via quantum scrambling [27, 28] and a backward denoising process via quantum measurement. We provide bounds on the learning error and then demonstrate QuDDPM's capability in examples relevant to characterizing quantum device noises, learning quantum many-body phases and capturing topological structure of quantum data. For an n -qubit problem, QuDDPM adopts linear-in- n layers of circuits to guarantee expressivity, while introduces $T \sim n/\log(n)$ intermediate training tasks and to guarantee efficient training.

* xiaohuic@usc.edu

† qzhuang@usc.edu

I. GENERAL FORMULATION OF QUDDPM

We consider the task of the generating new elements from an unknown distribution \mathcal{E}_0 of quantum states, provided only a number of samples $\mathcal{S}_0 = \{|\psi_k\rangle\} \sim \mathcal{E}_0$ from the distribution. Such a state generation task appears in various applications. For example, when a quantum device experiences random coherent errors, it produces a distribution of quantum states in a computation. Learning the potentially correlated and complex coherent errors in a multi-qubit system is important for quantum device calibration, benchmark and testing, and has recently received much attention [29, 30]. Another example is when quantum sensor networks [31, 32] send quantum probes to sense unitary physical process, on the return side the receiver will collect a pure state from a distribution in the ideal case. Furthermore, the distribution can also be quantum states encoding classical data, where QuDDPM can also process classical data.

To complete the task, QuDDPM learns a map from a noisy unstructured distribution of states to the structured target distribution \mathcal{E}_0 . It does so via a divide-and-conquer strategy of creating smooth interpolations between the target distribution and the full noisy distribution, so that the training is divided to sub-tasks of low-depth circuit to avoid barren plateau [33–36].

As shown in Fig. 1, QuDDPM includes two quantum circuits, one to enable the forward diffusion of sample data towards noise via scrambling and one to realize the backward denoising from noise towards generated data via measurement. For each data $|\psi_i^{(0)}\rangle$, the forward scrambling circuit (Fig. 1a) samples a series of T random unitary gates $U_1^{(i)}, \dots, U_T^{(i)}$ independently, such that the ensemble $\mathcal{S}_k = \{|\psi_i^{(k)}\rangle = \prod_{\ell=1}^k U_\ell^{(i)} |\psi_i^{(0)}\rangle\}_i$ evolves from the sample data towards a random ensemble of pure states from $k = 0$ to $k = T$. A Bloch sphere visualization of such a forward scrambling dynamics is depicted in Fig. 1(b1-b5) for a toy problem of learning single-qubit states clustered around a single pure state e.g. $|0\rangle$, where \mathcal{S}_0 is clustered around the north pole (b1) and \mathcal{S}_T is uniform on Bloch sphere (b5).

With the interpolation from data \mathcal{S}_0 and noise \mathcal{S}_T in hand, the backward process can start from randomly sampled noise $\tilde{\mathcal{S}}_T$ (Fig. 1c5) and reduce the noise gradually via measurement step by step, towards the final generated data $\tilde{\mathcal{S}}_0$ (Fig. 1c1) that mimic the sample data (Fig. 1b1). Measurements are necessary, as the denoising map needs to be contractive and maintain the purity of each generated data in $\tilde{\mathcal{S}}_0$. As shown in Fig. 1d, each denoising step adopts a unitary \tilde{U}_k on n_A number of ancilla qubits in $|0\rangle$ and performs a projective measurement in computational bases on the ancilla after the unitary \tilde{U}_k . Starting from the state $|\tilde{\psi}_i^{(T)}\rangle$, which is randomly sampled from entire noise, each unitary plus measurement step evolves the random state towards the generated data $|\tilde{\psi}_i^{(0)}\rangle$. Note that here all unitaries \tilde{U}_k are fixed after training. In practice, the generation of the fully noisy

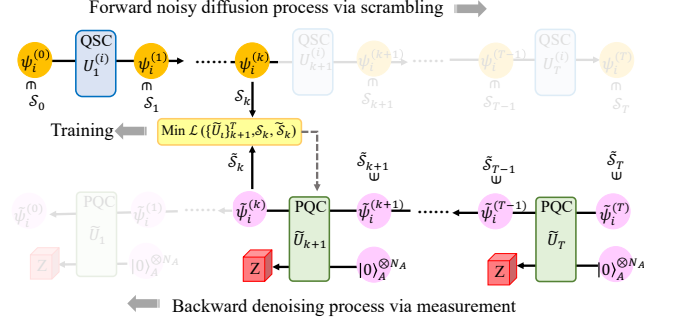


Figure 2. The training of QuDDPM at each step $t = k$. Pairwise distance between states in generated ensemble $\tilde{\psi}_i^{(k)} \in \tilde{\mathcal{S}}_k^{\text{tr}}$ and true diffusion ensemble $\psi_j^{(k)} \in \mathcal{S}_k$ is measured and utilized in the evaluation of the loss function \mathcal{L} .

state $|\tilde{\psi}_i^{(T)}\rangle$ can be directly completed by running the T layers of forward scrambling circuit.

II. TRAINING STRATEGY

In classical DDPM, the Gaussian nature of the diffusion allows efficient training via maximizing an evidence lower bound (ELBO) for the log-likelihood function, which can be evaluated *analytically* [18, 19] (see Appendix). However, in QuDDPM, we do not expect such analytical simplification to exist at all—classical simulation of quantum device is inherently inefficient. Instead, the training of the QuDDPM relies on the capability of quantum measurements to extract information about ensemble of quantum states for the efficient evaluation of a cost function.

The training of the QuDDPM with T steps consists of T training cycles, starting from the first denoising step \tilde{U}_T towards the last \tilde{U}_1 . As shown in Fig. 2, at the training cycle $(T + 1 - k)$, the forward noisy diffusion process is implemented from $U_1^{(i)}$ to $U_k^{(i)}$ to generate the noisy ensemble $\mathcal{S}_k = \{|\psi_i^{(k)}\rangle\}_i$. While the backward denoising process performs the denoising steps \tilde{U}_T to \tilde{U}_{k+1} to generate the denoising ensemble $\tilde{\mathcal{S}}_k = \{|\tilde{\psi}_i^{(k)}\rangle\}_i$. Within the training cycle, the parameters of the denoising PQC \tilde{U}_{k+1} is updated such that the generated denoising ensemble $\tilde{\mathcal{S}}_k$ converges to the noisy ensemble \mathcal{S}_k . Therefore, QuDDPM divides the original training problem into T smaller and easier ones. Indeed, even with a global cost function, we can divide the $\Omega(n)$ layers (required by expressivity) of gates to $T \in \Omega(n/\log n)$ diffusion steps, such that each \tilde{U}_{k+1} has order $\log(n)$ layers of gates to avoid barren plateau [34]. An explicit example where increasing T improves training is in the Appendix.

III. COST FUNCTION

To enable the training, we introduce a loss function to quantify the distance between the two ensembles of quantum states. In this work, we focus on the Maximum Mean Discrepancy (MMD) [38] and the Wasserstein distance [39, 40] based on the state overlaps $|\langle \psi_i^{(k)} | \tilde{\psi}_i^{(k)} \rangle|^2$ estimated via a swap test (see Appendix).

Given two independent distributions of pure states \mathcal{E}_1 and \mathcal{E}_2 on the state vector space V . The *state-wise fidelity* between $|\psi\rangle$ and $|\phi\rangle$ is defined as $F(|\phi\rangle, |\psi\rangle) = |\langle \phi | \psi \rangle|^2$, and we can further define the *mean fidelity* as

$$\bar{F}(\mathcal{E}_1, \mathcal{E}_2) = \mathbb{E}_{|\phi\rangle \sim \mathcal{E}_1, |\psi\rangle \sim \mathcal{E}_2} [|\langle \phi | \psi \rangle|^2], \quad (1)$$

where the random states $|\phi\rangle \sim \mathcal{E}_1$ and $|\psi\rangle \sim \mathcal{E}_2$ are drawn independently. Since the fidelity F is a symmetric and positive definite quadratic kernel, according to the theory of reproducing kernel Hilbert space (RKHS), the MMD distance can be written as (see Appendix)

$$\mathcal{D}_{\text{MMD}}(\mathcal{E}_1, \mathcal{E}_2) = \bar{F}(\mathcal{E}_1, \mathcal{E}_1) + \bar{F}(\mathcal{E}_2, \mathcal{E}_2) - 2\bar{F}(\mathcal{E}_2, \mathcal{E}_1), \quad (2)$$

which allows the estimation of MMD through sampled state ensembles \mathcal{S}_1 and \mathcal{S}_2 . It is clear that the expressivity of MMD as a statistical distance measure depends on the kernel. On one hand, identifiability requires, $\mathcal{L}_{\text{MMD}}(\mathcal{E}_1, \mathcal{E}_2) = 0$ if and only if $\mathcal{E}_1 = \mathcal{E}_2$. On the other hand, one also needs to ensure the quality of statistical estimation of the resulting MMD with finite sample size of state ensembles. Hence, whether fidelity (1) is a proper kernel choice is problem-dependent. In Appendix, we show an example where MMD fails to distinguish two simple distribution.

To resolve such an issue, we may alternatively consider the Wasserstein distance, a geometrically meaningful distance for comparing complex data distributions based on the theory of optimal transport [39, 40]. For pure states, choosing the quantum trace distance (equaling infidelity) $D^2(|\phi\rangle, |\psi\rangle) = 1 - |\langle \phi | \psi \rangle|^2$, then Kantorovich's formulation for optimal transportation is to solve the following optimization problem

$$\text{OPT} := \min_{\pi \in \Pi(\mathcal{E}_1, \mathcal{E}_2)} \int_{V \times V} D^p(|\phi\rangle, |\psi\rangle) d\pi(|\phi\rangle, |\psi\rangle) \quad (3)$$

for $p \geq 1$, where $\Pi(\mathcal{E}_1, \mathcal{E}_2)$ is the set of admissible *transport plans* (i.e., *couplings*) of probability distributions on $V \times V$ such that $\pi(B \times V) = \mathcal{E}_1(B)$ and $\pi(V \times B) = \mathcal{E}_2(B)$ for any measurable $B \subset V$; namely $\Pi(\mathcal{E}_1, \mathcal{E}_2)$ stands for all distributions with marginals as \mathcal{E}_1 and \mathcal{E}_2 . The Kantorovich problem in (3) induces a metric, known as the *p-Wasserstein distance*, on the space $\mathcal{P}_p(V)$ of probability distributions on V with finite p -th moment. In particular, the p -Wasserstein distance $W_p(\mathcal{E}_1, \mathcal{E}_2) = \text{OPT}^{1/p}$, and it has identifiability in the sense that $W_p(\mathcal{E}_1, \mathcal{E}_2) = 0$ if and only if $\mathcal{E}_1 = \mathcal{E}_2$. More details can be found in Appendix.

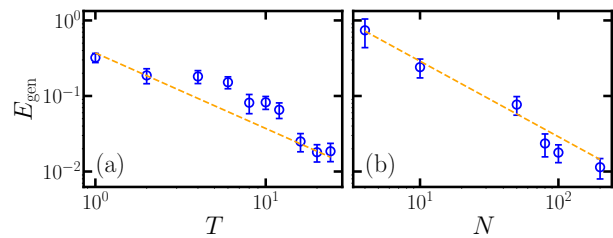


Figure 3. The generalization error of QuDDPM in generating cluster states versus (a) diffusion steps T and (b) training dataset size N . Dots are numerical results and orange dashed line is linear fitting results with both exponents equal to 1 within the numerical precision.

As shown in Fig. 2, in the training cycle $t = k$, loss is a function of the unitary $\{\tilde{U}_\ell\}_{k+1}^T$ and depends on the noise distribution $\tilde{\mathcal{E}}_T$ and the scrambled data distribution \mathcal{E}_k ,

$$\mathcal{L}(\{\tilde{U}_\ell\}_{k+1}^T, \mathcal{E}_k, \tilde{\mathcal{E}}_T) = \mathcal{D}(\mathcal{E}_k, \tilde{\mathcal{E}}_k[\{\tilde{U}_\ell\}_{k+1}^T, \tilde{\mathcal{E}}_T]), \quad (4)$$

where \mathcal{D} can be the MMD distance \mathcal{D}_{MMD} or the Wasserstein distance W_p . The distribution $\tilde{\mathcal{E}}_k$ is a function of all the reverse denoising steps and the noise distribution $\tilde{\mathcal{E}}_T$. In practice, we use finite samples to approximate the cost function as $\mathcal{L}(\{\tilde{U}_\ell\}_{k+1}^T, \mathcal{S}_k, \tilde{\mathcal{S}}_T)$.

IV. NUMBER OF GATES AND CONVERGENCE

Now we discuss about the number of local gates required and convergence analysis for the QuDDPM algorithm to solve an n -qubit generative task. For simplicity, we assume the qubits are one-dimensional with nearest neighbor interactions, while similar counting can be done for other cases. To guarantee convergence towards noise, the forward scrambling circuits needs number of layers linear in n as predicted by t -design [41, 42], leading to $O(n^2)$ total gates. The backward circuit will be similar, with at most $n_A \leq 2n$ additional ancillas and $O(n^2)$ gates, leading to the overall gate complexity of QuDDPM to be $O(n^2)$.

Similar to the classical case [43], the total error of QuDDPM involves three part,

$$E \simeq E_{\text{diff}} + E_{\mathcal{M}} + E_{\text{gen}}, \quad (5)$$

with deviation of \mathcal{S}_T to true random states E_{diff} , measurement error $E_{\mathcal{M}}$ and generalization error E_{gen} . We discuss the scaling of three part separately in the following. Suppose the diffusion circuits approach approximate K -design, its diffusion error is known as [41]

$$E_{\text{diff}} \sim 2^{nK} e^{-T/A(K)C} \sim \mathcal{O}(e^{-T}) \quad (6)$$

where $A(K) = \lceil \log_2(4K) \rceil^2 K^5 t^{3.1/\log(2)}$ is a polynomial of K and C is a constant determined by the circuit in a

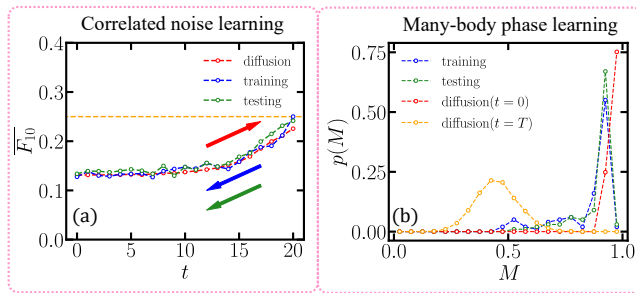


Figure 4. Generation of states with probabilistic correlated noise on a specific qubit state in (a) and (b) states with ferromagnetic phase. In (a), average fidelity \overline{F}_{10} between states at step t and $|10\rangle$ for forward diffusion (red), backward training (blue), backward test (green) are plotted. The shaded areas in blue and green show the sample standard deviation for backward training and test. In (b), we show the distribution of magnetization for generated data from training (blue) and testing (green) data set, and compared to true data (red) and full noise (orange). Four qubits are considered in (b).

single step. For measurement, the standard error in estimating the fidelity between any two states $|\psi_i\rangle, |\tilde{\psi}_j\rangle$ is $\text{SE}(F_{ij}) = \sqrt{(1 - F_{ij})/m}$, where m is the number of repetitions of measurement. With N data in the two sets $\mathcal{S}, \tilde{\mathcal{S}}$, the measurement error of estimating the *mean fidelity* is

$$E_{\mathcal{M}} = \frac{1}{N^2} \sqrt{\sum_{i,j=1}^N \text{SE}(F_{ij})^2} \sim \mathcal{O}\left(\frac{1}{N\sqrt{m}}\right). \quad (7)$$

Finally, we provide numerical evidence that the generalization error [44, 45]

$$E_{\text{gen}}(\{\tilde{U}_\ell\}_1^T) \equiv \mathcal{L}(\{\tilde{U}_\ell\}_1^T, \mathcal{E}_0, \tilde{\mathcal{E}}_T) - \mathcal{L}(\{\tilde{U}_\ell\}_1^T, \mathcal{S}_0, \tilde{\mathcal{S}}_T) \quad (8)$$

has the scaling $\mathcal{O}(\frac{1}{TN})$, as shown in Fig. 3 for a $n = 4$ qubit clustering state generation task. Here we estimate the generalization error via a validation set independently sampled. The $1/N$ scaling agrees with classical machine learning results [46, 47]. The full analyses of generalization error in unsupervised learning tasks is an open problem [44, 45].

V. APPLICATION EXAMPLES OF QUDDPM

Now we consider some generative learning applications to showcase QuDDPM. Towards this goal, we consider a particular realization of QuDDPM with each unitary $U_k^{(i)}$ and \tilde{U}_k implemented by the fast scrambling model [48] and hardware efficient ansatz separately (see Appendix). To test the performance after training, we randomly sample N_{test} random noise states, and perform the optimized backward PQC to generate the sampled data and evaluate the cost functions along the backward steps.

A. Clustered states generation: learning the noise

When a real quantum device is programmed to generate a quantum state, it inevitably suffers from errors in the gate control parameters. As a result, the states generated \mathcal{S}_0 are close to the target state but has nontrivial coherent errors, which can be learned by QuDDPM.

We begin with the simplest single-qubit scenario and define the target state as $|0\rangle$ to demonstrate QuDDPM. The forward scrambling and backward denoising processes have been explained earlier in Fig. 1, and we present the precise performance via fidelity F_0 with the state $|0\rangle$ and a two-qubit generalization in Appendix.

B. Learning correlated noise

To further connect to testing quantum devices, we consider the task of learning correlated noises, where each Pauli-string of error \mathbf{P} happen according to a nontrivial joint distribution. We take a two-qubit example of fully correlated noise, where $e^{-i\delta X_1 X_2}$ and $e^{-i\delta Z_1 Z_2}$ rotations happen with probability p and $1 - p$. Here X_k and Z_k are Pauli operator for qubit k . In each case, the angle of rotation δ is uniformly sampled from the range $[-\delta_0, \delta_0]$. To test the QuDDPM, we pick an initial state $|\Psi\rangle = c_0|00\rangle + c_1|01\rangle + c_3|11\rangle$ and consider the distribution of states generated by the fully correlated noise model above. As the $|10\rangle$ component in the superposition only appears when XX error happens, we can utilize average fidelity $\overline{F}_{10} = \mathbb{E}_{\tilde{\mathcal{S}}_0} |\langle 10 | \psi^{(0)} \rangle|^2$ as the performance metric to estimate the error probability p via $\tilde{p} = \overline{F}_{10} / (|c_1|^2 \mathbb{E}_\delta [\sin^2 \delta])$. We show a numerical example in Fig. 4(a), where the generated ensemble average fidelity in training and testing, agrees with the theoretical prediction up to a finite sample size deviation.

C. Learning many-body phases

We also extend applications of QuDDPM to the learning of many-body phases. We consider the generation of states with ferromagnetic phase. As a proof-of-principle, we take the simple and well-known transverse-field Ising model (TFIM) described by the Hamiltonian

$$H_{\text{TFIM}} = - \sum_i Z_i Z_{i+1} - g \sum_i X_i. \quad (9)$$

When g increases from zero, the system undergoes a phase transition from ordered ferromagnetic phase to disordered phase, with the critical point at $g = 1$. The states before diffusion is chosen from ground states of Eq. (9) with $g \in [0.2, 0.4]$ uniformly distributed. To test the capability of QuDDPM, we utilize the magnetization, $M = (\sum_i Z_i)/n$, to identify the phase of generated states from QuDDPM, and show its distribution in Fig. 4(b). Most generated states (blue and green) of QuDDPM lives

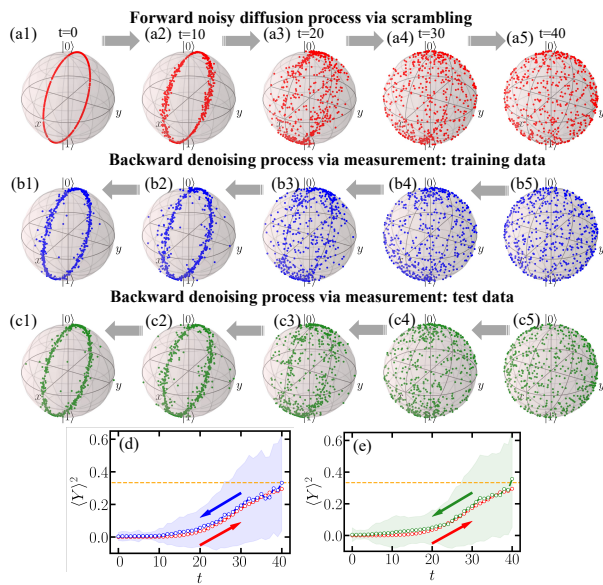


Figure 5. Bloch visualization of the forward (a1-a5) and backward (b1-b5,c1-c5) process. (d)(e) deviation of generated states from unit circle in $X-Z$ plane. The deviation $\langle Y \rangle^2$ for forward diffusion (red), backward training (blue), backward test (green) are plotted. The shaded area show the sample standard deviation.

in the ferromagnetic phase, and shows a sharp contrast to the random states (orange).

D. Nontrivial topology: learning the structure

We consider ensemble of states with a ring structure—generated by applying a unitary on a single state, e.g., $|\psi_i\rangle = e^{-i\mathbf{x}_i \cdot \mathbf{G}} |0\rangle$, which models the scenario where one encodes the classical data \mathbf{x}_i onto the quantum data ψ_i , as commonly adopted in quantum machine learning [16, 49–51] to solve classical problems. We test QuDDPM with a single qubit toy example, where the generators are chosen as Pauli-Y and the rotation angles uniform in $[0, 2\pi)$. In the QuDDPM training, we use the Wasserstein distance [40] to cope with the nontrivial topology. The forward noisy diffusion process on the sample data and the backward denoising process for training and testing are depicted in Fig. 5. To quantitatively evaluate the performance of QuDDPM, we evaluate the deviation by Pauli-Y expectation $\langle Y \rangle^2$ in Fig. 5(d)(e), where gradual transition between zero and Haar value of $1/3$ is observed in both forward diffusion and backward denoising.

VI. DISCUSSIONS

Below, we discuss about several related works. Ref. [52] utilizes diffusion map (DM) for unsupervised learning of topological phases and [53] proposes a diffu-

sion K -means manifold clustering approach based on the diffusion distance [54]. Quantum DM algorithm has also been considered [55] for potentially quantum speed-up. However, these works are not on generative learning and do not consider any denoising process. Layer-wise training [56] also attempts to divide a training problem into sub-tasks in non-generative learning; however, the performance of such strategies is limited [57]. QuDDPM integrates the division of training task and an actual noisy diffusion process to enable provable benefit in training.

The proposed QuDDPM represents a use case of theoretical idea of quantum information scrambling [27, 28] in the forward diffusion, and its backward denoising also connects to the measurement-induced phase transitions [58]. Finally, we point out some future directions, besides various applications of QuDDPM in learning quantum systems. Our current QuDDPM architecture requires a loss function based on fidelity estimations. For large systems, fidelity estimation can be challenging to implement. Towards efficient training in large systems, alternative loss functions can be adopted. For example, one may consider adopting another quantum circuit trained for telling the ensembles apart, such as quantum convolutional neural network [7] and other circuit architecture [59]. Such an approach will combine QuDDPM and the adversarial agent in QuGAN to resolve training problem in QuGAN. Another future direction is controlled diffusion [60]: when the ensemble has special symmetry, one can restrict the forward scrambling, the backward denoising and the random noise ensemble to that symmetry.

ACKNOWLEDGMENTS

QZ and BZ acknowledges support from NSF CAREER Award CCF-2240641 and ONR N00014-23-1-2296. XC acknowledges support from NSF CAREER Award DMS-2347760.

Appendix A: Details of parameters

We list hyperparameters and performance for all generative learning tasks in Table I for reference, and state the targeted distribution of states to generate in the following.

In Fig. 1(b)(c), we consider data in the form of $|\psi^{(0)}\rangle \sim |0\rangle + \epsilon c_1 |1\rangle$ up to a normalization constant where $\text{Re}\{c_1\}, \text{Im}\{c_1\} \sim \mathcal{N}(0, 1)$ is Gaussian distributed and the scale factor is chosen $\epsilon = 0.08$. We have taken single qubit rotations as $U_k^{(i)}$, where each angle is randomly sampled, e.g., from the uniform distribution $U[-\pi/8, \pi/8]$. In the generation of states with probabilistic correlated noise of Fig. 4(a), the noise perturbation range is $\delta \in [-\pi/3, \pi/3]$.

Generation task	n	n_A	L	T	N	Cost func.	Performance
Clustered state (Fig. 1 and Fig. 10a)	1	1	4	20	100	MMD	$\overline{F_{0,\text{data}}} = 0.987 \pm 0.013$ $\overline{F_{0,\text{tr}}} = 0.992 \pm 0.021$ $\overline{F_{0,\text{te}}} = 0.993 \pm 0.014$
Clustered state (Fig. 10b)	2	1	6	20	100	MMD	$\overline{F_{0,\text{data}}} = 0.977 \pm 0.014$ $\overline{F_{0,\text{tr}}} = 0.952 \pm 0.070$ $\overline{F_{0,\text{te}}} = 0.944 \pm 0.075$
Clustered state (Fig. 3a and 3b)	4	2	8	20 (Fig. 3b)	100 (Fig. 3a)	MMD	see Fig. 3a and 3b
Correlated noise (Fig. 4a)	2	2	6	20	500	MMD	data: 0.129 training: 0.128 testing: 0.133
Many-body phase (Fig. 4b)	4	2	12	30	100	MMD	data: 1 training: 0.9 testing: 0.96
Circular states (Fig. 5)	1	2	6	40	500	Wasserstein	data: $\langle Y \rangle^2 = 0$ training: $\langle Y \rangle^2 = 0.00367 \pm 0.0251$ testing: $\langle Y \rangle^2 = 0.00506 \pm 0.0439$

Table I. List of hyperparameters of QuDDPM and its performance in different generative learning tasks. Data set size $N_{\text{tr}} = N_{\text{te}} = N$. n is the number of data qubit n and n_A the ancilla qubit. L is the PQC depth. T is the diffusion steps.

Appendix B: Appendix on comparison to quantum direct transport

Here we compare the performance between QuDDPM and quantum direct transport (QuDT). QuDT utilizes the same setup as QuDDPM, but attempts to generate the target state ensemble from a random state ensemble directly by only one PQC with L_{DT} layers (see Fig. 6(a)). Note that due to the single-step operation, the forward noisy diffusion process is not necessary to implement. For a fair comparison, the PQC in QuDT works on the same number of data and ancilla qubits and has the same total number of layers of circuits $L_{\text{DT}} = TL$ as the QuDDPM. The difference is that QuDDPM adopts forward diffusion combining backward denoising with T steps. We show the performance of QuDT in generating clustered and ring-structured state ensemble in Fig. 6(bottom). Compared to the performance of QuDDPM, QuDT presents a much larger deviation to the target state ensemble in both cases, which indicates the necessity of having multiple denoising steps to improve the capability of QuDDPM. The minimum number of denoising steps to obtain the optimal performance, and the scaling of performance with respect to diffusion steps T are subject to future study.

Appendix C: Review of Classical DDPM

Classical DDPM can be viewed as a latent variational autoencoder (VAE) model with stochastic hidden layers of the same dimension as the input data. The forward diffusion process simply adds a sequence of small amount of Gaussian perturbations to the data sample x_0 in T

steps to produce the noisy samples x_1, \dots, x_T according to a linear Markov chain:

$$q(x_t | x_{t-1}) = N(x_t | \sqrt{1 - \beta_t}x_{t-1}, \beta_t I),$$

where $\beta_t \in (0, 1)$ is a noise schedule such that $q(x_t)$ converges to $N(0, I)$. Usually the noise schedule satisfies $\beta_1 < \beta_2 < \dots < \beta_T$ so that larger step sizes are used when the samples become more noisy. In the time-reversal process, we would like to sample from $q(x_{t-1} | x_t)$, which allows us to generate new data sample from the noise distribution $q(x_T)$. However, the conditional distribution $q(x_{t-1} | x_t)$ is intractable and approximated by a decoder of the form:

$$p_\theta(x_{t-1} | x_t) = N(x_{t-1} | \mu_\theta(x_t, t), \sigma_t^2 I),$$

where the time-dependent conditional mean vector μ_θ is parameterized by a neural network. Then the training of μ_θ can be efficiently performed by maximizing an evidence lower bound (ELBO) for the log-likelihood function $\log p_\theta(x_0)$. Refs. [18, 19] showed that the ELBO can be expressed as a linear combination of (relative) entropy terms for Gaussian distributions that can be evaluated analytically into a simple weighted L^2 loss function.

Appendix D: Reproducing kernel Hilbert spaces and maximum mean discrepancy

A bivariate function $F : V \times V \rightarrow \mathbb{R}$ is a positive definite kernel if $\sum_{i,j=1}^m c_i c_j F(|\phi\rangle_i, |\phi\rangle_j) \geq 0$ for all $m \geq 1$, $|\phi\rangle_1, \dots, |\phi\rangle_m \in V$, and $c_1, \dots, c_m \in \mathbb{R}$. From the Moore-Aronszajn theorem (see e.g., [61, Theorem 7.2.4]), for every symmetric and positive-definite kernel F , there

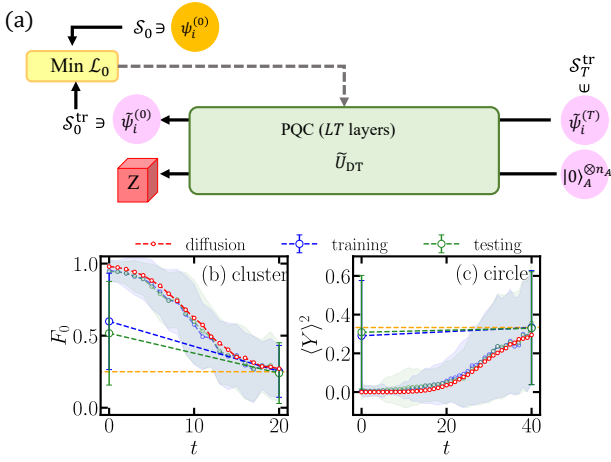


Figure 6. Schematic and performance of QuDT in state ensemble generation. Since the forward of QuDT only has a single step to noise, it is not necessary to implement. In backward process, there is also a single PQC \tilde{U}_{DT} with depth LT . In the training, the samples generated via applying \tilde{U}_{DT} on random states are directly compared to the target ensemble \mathcal{S}_0 , shown in (a). In the bottom panel, we show the performance of QuDT to generate (b) clustered state around $|0,0\rangle$ with $L_{DT} = 80$ and (c) circular state ensemble with $L_{DT} = 240$. Blue and green dots with error bar represents the mean and standard deviation of samples generated by QuDT in training and test. All other parameters and distance choice is same as the ones used in QuDDPM, see Fig. 5. The dotted line with shaded areas in background are QuDDPM performance for comparison.

is a unique Hilbert space $\mathcal{H} := \mathcal{H}(F)$ of real-valued functions on V such that:

- (i) $F(\cdot, |\phi\rangle) \in \mathcal{H}$ for each $|\phi\rangle \in V$;
- (ii) $g(|\phi\rangle) = \langle g, F(\cdot, |\phi\rangle) \rangle_{\mathcal{H}}$ for each $g \in \mathcal{H}$ and $|\phi\rangle \in V$.

The space \mathcal{H} of functions $\{g : V \rightarrow \mathbb{R}\}$ is called the reproducing kernel Hilbert space (RKHS) associated with the kernel F . Property (i) defines a feature map (a.k.a. RKHS map) $V \rightarrow \mathcal{H}$ via $|\phi\rangle \mapsto F(\cdot, |\phi\rangle)$, and property (ii) is the reproducing kernel property for the evaluation functionals. In addition, we have for all $|\phi\rangle, |\psi\rangle \in V$,

$$F(|\phi\rangle, |\psi\rangle) = \langle F(\cdot, |\psi\rangle), F(\cdot, |\phi\rangle) \rangle_{\mathcal{H}} = |\langle \phi | \psi \rangle|^2.$$

Based on the kernel F , the (squared) maximum mean discrepancy (MMD) loss between two state distributions is

$$\begin{aligned} \mathcal{D}_{\text{MMD}}(\mathcal{E}_1, \mathcal{E}_2) & := \sup_{g \in \mathcal{B}} |\langle \mathbb{E}_{|\phi\rangle \sim \mathcal{E}_1} [F(\cdot, |\phi\rangle)] - \mathbb{E}_{|\psi\rangle \sim \mathcal{E}_2} [F(\cdot, |\psi\rangle)], g \rangle_{\mathcal{H}}|^2, \end{aligned} \quad (\text{D1})$$

where \mathcal{B} is the unit ball in \mathcal{H} centered at the origin and $\langle \cdot, \cdot \rangle_{\mathcal{H}}$ denotes the inner product in the RKHS.

By duality of \mathcal{H} , we have

$$\begin{aligned} \mathcal{D}_{\text{MMD}}(\mathcal{E}_1, \mathcal{E}_2) & = \|\mathbb{E}_{|\phi\rangle \sim \mathcal{E}_1} [F(\cdot, |\phi\rangle)] - \mathbb{E}_{|\psi\rangle \sim \mathcal{E}_2} [F(\cdot, |\psi\rangle)]\|_{\mathcal{H}}^2. \end{aligned}$$

Therefore, we may calculate the MMD loss as following

$$\begin{aligned} \mathcal{D}_{\text{MMD}}(\mathcal{E}_1, \mathcal{E}_2) & = \langle \mathbb{E}_{|\phi\rangle \sim \mathcal{E}_1} [F(\cdot, |\phi\rangle)], \mathbb{E}_{|\phi'\rangle \sim \mathcal{E}_1} [F(\cdot, |\phi'\rangle)] \rangle_{\mathcal{H}} \\ & \quad + \langle \mathbb{E}_{|\psi\rangle \sim \mathcal{E}_2} [F(\cdot, |\psi\rangle)], \mathbb{E}_{|\psi'\rangle \sim \mathcal{E}_2} [F(\cdot, |\psi'\rangle)] \rangle_{\mathcal{H}} \\ & \quad - 2 \langle \mathbb{E}_{|\phi\rangle \sim \mathcal{E}_1} [F(\cdot, |\phi\rangle)], \mathbb{E}_{|\psi\rangle \sim \mathcal{E}_2} [F(\cdot, |\psi\rangle)] \rangle_{\mathcal{H}} \\ & = \mathbb{E}_{|\phi\rangle, |\phi'\rangle \sim \mathcal{E}_1} [F(|\phi\rangle, |\phi'\rangle)] \\ & \quad + \mathbb{E}_{|\psi\rangle, |\psi'\rangle \sim \mathcal{E}_2} [F(|\psi\rangle, |\psi'\rangle)] \\ & \quad - 2 \mathbb{E}_{|\phi\rangle \sim \mathcal{E}_1, |\psi\rangle \sim \mathcal{E}_2} [F(|\phi\rangle, |\psi\rangle)], \end{aligned}$$

where all random states $|\phi\rangle, |\phi'\rangle, |\psi\rangle, |\psi'\rangle$ are drawn independently. Hence, we have established the connection

$$\mathcal{D}_{\text{MMD}}(\mathcal{E}_1, \mathcal{E}_2) = \overline{F}(\mathcal{E}_1, \mathcal{E}_1) + \overline{F}(\mathcal{E}_2, \mathcal{E}_2) - 2\overline{F}(\mathcal{E}_1, \mathcal{E}_2),$$

where $\overline{F}(\mathcal{E}_1, \mathcal{E}_2) := \mathbb{E}_{|\phi\rangle \sim \mathcal{E}_1, |\psi\rangle \sim \mathcal{E}_2} [F(|\phi\rangle, |\psi\rangle)]$. In particular, if $F = |\langle \phi | \psi \rangle|^2$ is state-wise fidelity, then the resulting MMD corresponds to the mean fidelity defined in Eq. (1) of the main text.

Appendix E: Computation of Wasserstein distance.

In the discrete or empirical cases, where \mathcal{S}_1 and \mathcal{S}_2 are supported over finite number of state vectors $\{|\phi_i\rangle\}_{i=1}^m$ and $\{|\psi_j\rangle\}_{j=1}^n$, computation of Wasserstein distance can be cast into a linear program [62]. To this end, let a and b be histograms representing \mathcal{S}_1 and \mathcal{S}_2 , respectively. Define the $m \times n$ cost matrix C by $C_{i,j} := D^2(|\phi_i\rangle, |\psi_j\rangle)$, where $|\phi_i\rangle$ and $|\psi_j\rangle$ are state vectors from sampled ensemble state \mathcal{S}_1 and \mathcal{S}_2 , respectively. For pure states, the cost matrix reduces to a function of infidelity, i.e., $C_{i,j} = 1 - F^2(|\phi_i\rangle, |\psi_j\rangle)$. Then we have

$$\begin{aligned} W_2(\mathcal{S}_1, \mathcal{S}_2) & = \min_P \langle P, C \rangle, \\ \text{s.t.} \quad & P \mathbf{1}_n = a, \\ & P^\top \mathbf{1}_m = b, \\ & P \geq 0. \end{aligned}$$

Furthermore, we note that the above generalization of Wasserstein distance to characterize separation between two ensembles of quantum states is different from the case of Refs. [63–65], where only a pair of quantum states are considered.

Appendix F: SWAP test

In the QuDDPM framework in the main text, we need to evaluate the fidelities between states $|\psi\rangle$ from real diffusion ensemble $\tilde{\mathcal{S}}_k$ and the ones $|\tilde{\psi}\rangle$ from backward generated ensemble $\tilde{\mathcal{S}}_k$. For any two pure states $|\psi\rangle$ and $|\tilde{\psi}\rangle$,

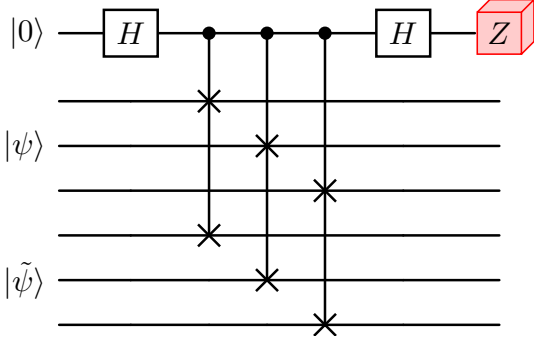


Figure 7. Circuit implementation of swap test. We show an example of swap test between two 3-qubit state $|\psi\rangle, |\tilde{\psi}\rangle$. A Z-basis measurement is performed at the end.

one can perform the SWAP test to obtain the fidelity, which is illustrated in Fig. 7. The SWAP test consists of two Hadamard gate and a controlled-swap gate applied on $2n + 1$ qubits. Given the input $|0, \psi, \tilde{\psi}\rangle$, the output state ahead of measurement is

$$\begin{aligned} |0, \psi, \tilde{\psi}\rangle &\rightarrow \frac{1}{2} |0\rangle \left(|\psi, \tilde{\psi}\rangle + |\tilde{\psi}, \psi\rangle \right) \\ &+ \frac{1}{2} |1\rangle \left(|\psi, \tilde{\psi}\rangle - |\tilde{\psi}, \psi\rangle \right), \end{aligned} \quad (\text{F1})$$

then the probability of measure 0 on the first qubit is

$$\begin{aligned} P(\text{first qubit in } |0\rangle) &= \frac{1}{4} \left(\langle\psi, \tilde{\psi}| + \langle\tilde{\psi}, \psi| \right) \left(|\psi, \tilde{\psi}\rangle + |\tilde{\psi}, \psi\rangle \right) \\ &= \frac{1}{2} + \frac{1}{2} |\langle\psi|\tilde{\psi}\rangle|^2 \end{aligned} \quad (\text{F2})$$

which directly indicates the fidelity. To implement the swap test between two n -qubit state $|\psi\rangle$ and $|\tilde{\psi}\rangle$, in general we need n Fredkin gate between every pair of qubits of $|\psi\rangle$ and $|\tilde{\psi}\rangle$, where it is sufficient to implement a Fredkin gate among a control qubit and two target qubits via 5 two-qubit gate [66]. Therefore, in general $\mathcal{O}(5n)$ two-qubit gates are enough to perform the swap test in Fig. 7 regardless the locality of these gates.

Appendix G: Forward and backward circuits

The forward noisy process is implemented by the fast scrambling model [48] with controllable parameters on n data qubits to mimic the diffusion process in the Hilbert space. The diffusion circuit is implemented as (see Fig. 8 (a))

$$U(\phi_t, g_t) = \prod_{t=1}^T W_t(g_t) V_t(\phi_t), \quad (\text{G1})$$

where V_t consists of general single qubit rotations on each qubit as

$$V_t(\phi_t) = \bigotimes_{k=1}^n e^{-i\phi_t, 3k+2} Z_k / 2 e^{-i\phi_t, 3k+1} Y_k / 2 e^{-i\phi_t, 3k} Z_k / 2, \quad (\text{G2})$$

and homogeneous entangling layer W_t consists of ZZ rotation on every pair of qubits,

$$\begin{aligned} W_t(g_t) &= \exp \left[-i \frac{g_t}{2\sqrt{n}} \sum_{k_1 < k_2} Z_{k_1} Z_{k_2} \right] \\ &= \prod_{k_1 < k_2} \exp \left[-i \frac{g_t}{2\sqrt{n}} Z_{k_1} Z_{k_2} \right]. \end{aligned} \quad (\text{G3})$$

With a tunable range of random rotation angles ϕ and g , we can control the diffusion speed of original quantum states ensemble \mathcal{S}_0 in the Hilbert space towards Haar random states ensemble.

The backward denoising process consists of T steps, where the operation at every step is implemented by a PQC $\tilde{U}_t(\theta_t)$ followed by measurements on ancillas.

$$\begin{aligned} \Phi_t \left(|\tilde{\psi}^{(t)}\rangle \right) &= \frac{(\Pi_A \otimes \mathbf{I}_D) \tilde{U}_t |\tilde{\psi}^{(t)}\rangle}{\sqrt{\langle\tilde{\psi}^{(t)}|\tilde{U}_t^\dagger (\Pi_A \otimes \mathbf{I}_D) \tilde{U}_t |\tilde{\psi}^{(t)}\rangle}} \\ &= |z(t)\rangle_A \otimes |\tilde{\psi}^{(t-1)}\rangle \end{aligned} \quad (\text{G4})$$

where $\Pi_A = |z(t)\rangle\langle z(t)|_A$ is the POVM of measurement on ancillas in computational basis $|z(t)\rangle_A$. Note that we do not make any specific constraint on the measurement results $z(t)$, instead, we simply perform the measurement on ancillas and collect post-measurement state on data qubits $|\tilde{\psi}^{(t-1)}\rangle$.

In general, the backward PQC can utilize any architecture as long as its expressivity can guarantee for the backward transport from ensemble \mathcal{S}_{t+1} to \mathcal{S}_t . In this work, we adopt the hardware-efficient ansatz which is universal and easy to implement in practical experiments. For a L -layer backward PQC \tilde{U}_t , in each layer it consists of single qubits rotations along X and Y axes on each qubit, followed by control-Z gate on nearest neighbors as (see Fig. 8 (b))

$$\tilde{U}_t(\theta_t) = \prod_{\ell=1}^L \tilde{W}_t \tilde{V}_t(\theta_t) \quad (\text{G5})$$

where

$$\begin{aligned} \tilde{V}_t(\theta_t) &= \bigotimes_{k=1}^n e^{-i\theta_t, 2k+1} Y_k / 2 e^{-i\theta_t, 2k} X_k / 2 \\ \tilde{W}_t &= \bigotimes_{k=1}^{\lfloor (n-1)/2 \rfloor} \text{CZ}_{2k, 2k+1} \bigotimes_{k=1}^{\lfloor n/2 \rfloor} \text{CZ}_{2k-1, 2k} \end{aligned} \quad (\text{G6})$$

with CZ_{k_1, k_2} to be the control-Z gate on qubit k_1 and k_2 .

The whole backward denoising process can thus be represented as

$$\Phi = \Phi_1 \circ \Phi_2 \circ \dots \circ \Phi_{T-1} \circ \Phi_T. \quad (\text{G8})$$

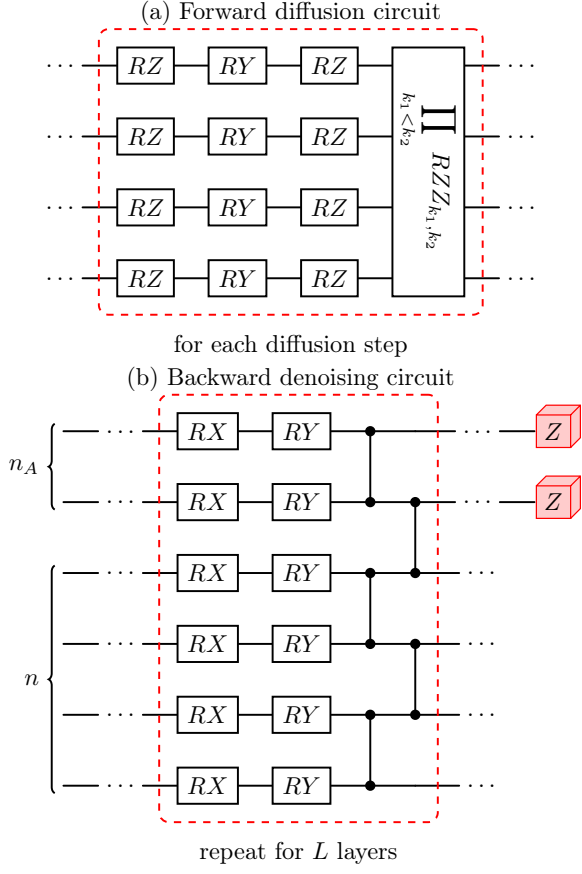


Figure 8. Quantum circuit architectures. In (a) we show the forward diffusion circuit for one diffusion step on a system of $n = 4$ qubits. In (b) we show one-layer architecture of a L -layer backward denoising PQC on a system of $n = 4$ data and $n_A = 2$ ancilla qubits. RX, RY and RZ are Pauli X, Y and Z rotations. RZZ is the two-qubit ZZ rotation.

Appendix H: Additional details on distance metrics evaluation

In Fig. 9, we show a numerical comparison between the MMD distance (see Eq. 2) and Wasserstein distance (see Eq. 3) in different generation tasks. In the clustered state generation (Fig. 9(a), (b)), both distance measure behaves similarly. However, for the circular state generation in Fig. 9(c), (d), the Wasserstein distance can characterize the diffusion of ensemble while the MMD distance fails. Note that only relative shift of MMD or Wasserstein loss through diffusion matters, while a comparison between their magnitude is unfair. In the following, we provide the simple proof on Lemma 1.

Lemma 1 *Let \mathcal{E}_1 be a uniform circular distribution on the Bloch sphere and \mathcal{E}_2 be the Haar random state distribution. Then $\mathcal{D}_{\text{MMD}}(\mathcal{E}_1, \mathcal{E}_2) = 0$.*

Proof of Lemma 1. We can calculate the ensemble

average fidelity by Haar integral as

$$\begin{aligned} \overline{F}(\mathcal{E}_1, \mathcal{E}_2) &= \frac{1}{2\pi} \int_0^{2\pi} d\theta \int dU |\langle 0|U^\dagger e^{-i\theta Y}|0\rangle|^2 \\ &= \frac{1}{2\pi} \int d\theta \frac{\text{tr}(|0\rangle\langle 0|) \text{tr}(e^{-i\theta Y} |0\rangle\langle 0| e^{i\theta Y})}{2} \\ &= \frac{1}{2}, \\ \overline{F}(\mathcal{E}_1, \mathcal{E}_1) &= \frac{1}{(2\pi)^2} \int_0^{2\pi} d\theta d\theta' |\langle 0|e^{i\theta' Y} e^{-i\theta Y}|0\rangle|^2 \\ &= \frac{1}{(2\pi)^2} \int_0^{2\pi} d\theta d\theta' \cos^2(\theta' - \theta) \\ &= \frac{1}{2}, \\ \overline{F}(\mathcal{E}_2, \mathcal{E}_2) &= \int dU dU' |\langle 0|U^\dagger U'|0\rangle|^2 \\ &= \int dU \frac{\text{tr}(|0\rangle\langle 0|) \text{tr}(U |0\rangle\langle 0| U^\dagger)}{2} \\ &= \frac{1}{2}. \end{aligned}$$

Therefore, the MMD distance is

$$\mathcal{D}_{\text{MMD}}(\mathcal{E}_1, \mathcal{E}_2) = \overline{F}(\mathcal{E}_1, \mathcal{E}_1) + \overline{F}(\mathcal{E}_2, \mathcal{E}_2) - 2\overline{F}(\mathcal{E}_1, \mathcal{E}_2) = 0, \quad (\text{H1})$$

which indicates its incapability to discriminate the difference between the circular state ensemble and Haar random states. ■

For the true distribution, when $\mathcal{E}_1 = \mathcal{E}_2$, we should have $\mathcal{D}_{\text{MMD}}(\mathcal{E}_1, \mathcal{E}_2) = \mathcal{D}_{\text{Wass}}(\mathcal{E}_1, \mathcal{E}_2) = 0$ in theory, while

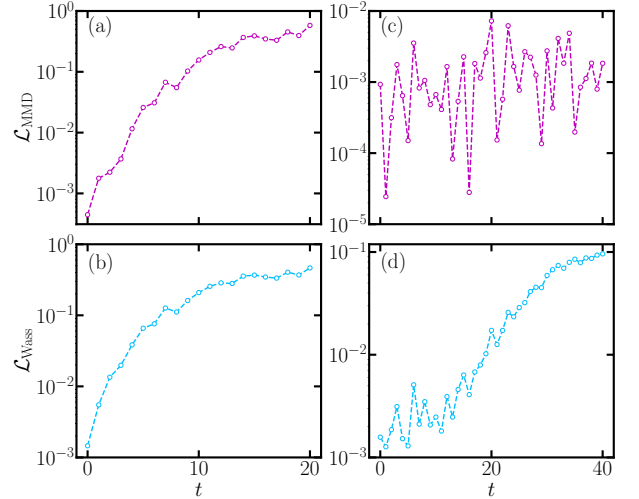


Figure 9. MMD and Wasserstein loss between ensemble \mathcal{S}_0 and ensemble through diffusion process at step t , \mathcal{S}_t in generation of cluster state (left) and circular state ensemble (right). For cluster state ensemble, MMD (a) and Wasserstein loss (c) behaves similarly. For circular state ensemble, MMD loss (c) vanishes while Wasserstein loss characterize the diffusion of distribution. The data set size for cluster states is $|\mathcal{S}| = 100$, and $|\mathcal{S}| = 500$ for circular states.

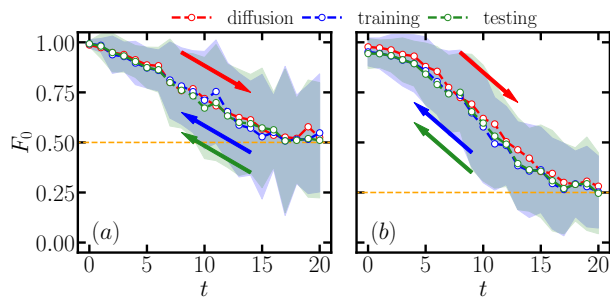


Figure 10. Dynamics of fidelity between generated states and $|0\rangle^{\otimes n}$ with (a) $n = 1$ and (b) $n = 2$ qubits. Average fidelity of diffusion (red), training (blue), testing (green) are plotted here with blue and green shaded area represent the standard deviation.

in practice due to finite samples, both of them cannot vanish exactly (see Fig. 9) left with a relatively small residual.

Appendix I: Details of clustered state generation

We provide more numerical details on the generation of clustered states. To understand the performance more directly, besides the cost function, we can utilize the overlap fidelity F_0 with the state $|0\rangle$ due to the clustering of the targeted data. In Fig. 10(a), the clustered data are same as in Fig. 1(b),(c) of the main text, and the forward scrambling decreases the fidelity (red dots) from unity towards towards the Haar random value of $\overline{F_0} = 1/2$ (yel-

low dashed) at $t = 20$. The backward denoising (blue dots) on the other hand reverses the fidelity evolution from $t = 20$ to $t = 0$, which is also verified by the test data (green dots). The above task can be extended to multiple qubits.

We also consider an distribution of two-qubit states clustered around $|0, 0\rangle$ for simplicity in multi-qubit clustered state generation. For $n = 2$, the data in the form of $|\psi^{(0)}\rangle \sim |0, 0\rangle + \epsilon(c_1|0, 1\rangle + c_2|1, 0\rangle + c_3|1, 1\rangle)$ up to a normalization constant where $\{c_i\}_{i=1}^3$ are all complex Gaussian distributed and the scale factor is chosen $\epsilon = 0.06$. We plot the fidelity with the state $|0, 0\rangle$ in Fig. 10(b) and the same evolution between ideal unity and Haar value of $1/4$ is confirmed.

Appendix J: Details of training

In this work, the simulation of QuDDPM is implemented with the Python library `TensorCircuit` [67] and Bloch sphere visualizations are plotted with the help from `QuTip` [68]. The computation of the Wasserstein distance, on the other hand, is performed by the Python library `POT` [69].

In Fig. 11, we show the training history of loss function in generating cluster state ensemble close to $|0, 0\rangle$, whose corresponding performance is in Fig. 10 (b) in the main text. The fluctuation in the training history of every denoising step is due to the random measurement in each training steps. In sample generation with optimized denoising PQC, the fluctuation is comparably small to the mean.

-
- [1] J. Biamonte, P. Wittek, N. Pancotti, P. Rebentrost, N. Wiebe, and S. Lloyd, *Nature* **549**, 195 (2017).
- [2] P. Rebentrost, M. Mohseni, and S. Lloyd, *Phys. Rev. Lett.* **113**, 130503 (2014).
- [3] S. Lloyd, M. Mohseni, and P. Rebentrost, *Nat. Phys.* **10**, 631 (2014).
- [4] M. Cerezo, A. Arrasmith, R. Babbush, S. C. Benjamin, S. Endo, K. Fujii, J. R. McClean, K. Mitarai, X. Yuan, L. Cincio, *et al.*, *Nature Reviews Physics* **3**, 625 (2021).
- [5] N. Killoran, T. R. Bromley, J. M. Arrazola, M. Schuld, N. Quesada, and S. Lloyd, *Phys. rev. res.* **1**, 033063 (2019).
- [6] A. Abbas, D. Sutter, C. Zoufal, A. Lucchi, A. Figalli, and S. Woerner, *Nat. Comput. Sci* **1**, 403 (2021).
- [7] I. Cong, S. Choi, and M. D. Lukin, *Nat. Phys.* **15**, 1273 (2019).
- [8] X. Gao, E. R. Anschuetz, S.-T. Wang, J. I. Cirac, and M. D. Lukin, *Phys. Rev. X* **12**, 021037 (2022).
- [9] A. Khoshaman, W. Vinci, B. Denis, E. Andriyash, H. Sadeghi, and M. H. Amin, *Quantum. Sci. Technol.* **4**, 014001 (2018).
- [10] M. H. Amin, E. Andriyash, J. Rolfe, B. Kulchytsky, and R. Melko, *Phys. Rev. X* **8**, 021050 (2018).
- [11] X. Gao, Z.-Y. Zhang, and L.-M. Duan, *Sci. Adv.* **4**, eaat9004 (2018).
- [12] I. Goodfellow, J. Pouget-Abadie, M. Mirza, B. Xu, D. Warde-Farley, S. Ozair, A. Courville, and Y. Bengio, in *Adv. Neural Inf. Process.*, Vol. 27, edited by Z. Ghahramani, M. Welling, C. Cortes, N. Lawrence, and K. Weinberger (Curran Associates, Inc., 2014).
- [13] S. Lloyd and C. Weedbrook, *Phys. Rev. Lett.* **121**, 040502 (2018).
- [14] P.-L. Dallaire-Demers and N. Killoran, *Phys. Rev. A* **98**, 012324 (2018).
- [15] L. Hu, S.-H. Wu, W. Cai, Y. Ma, X. Mu, Y. Xu, H. Wang, Y. Song, D.-L. Deng, C.-L. Zou, *et al.*, *Sci. Adv.* **5**, eaav2761 (2019).
- [16] H.-L. Huang, Y. Du, M. Gong, Y. Zhao, Y. Wu, C. Wang, S. Li, F. Liang, J. Lin, Y. Xu, *et al.*, *Phys. Rev. Appl* **16**, 024051 (2021).
- [17] E. Y. Zhu, S. Johri, D. Bacon, M. Esencan, J. Kim, M. Muir, N. Murgai, J. Nguyen, N. Plesch, A. Schouela, *et al.*, *Phys. rev. res.* **4**, 043092 (2022).
- [18] J. Sohl-Dickstein, E. Weiss, N. Maheswaranathan, and S. Ganguli, in *International conference on machine learning* (PMLR, 2015) pp. 2256–2265.
- [19] J. Ho, A. Jain, and P. Abbeel, *Adv. Neural Inf. Process.* **33**, 6840 (2020).

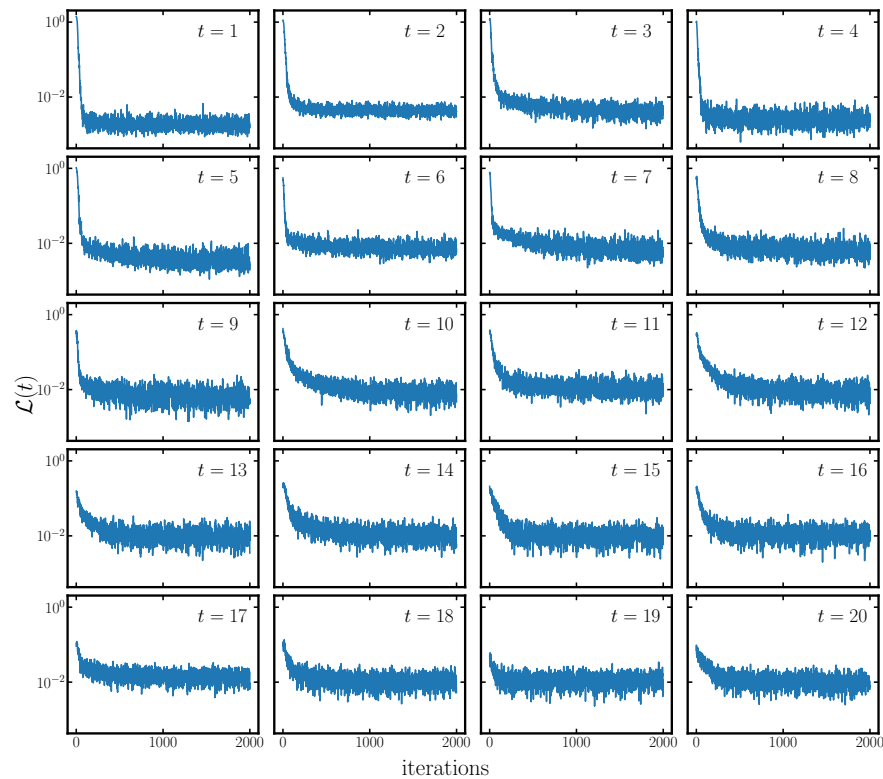


Figure 11. Training history of loss function in each denoising step for generating cluster state ensemble close to $|0, 0\rangle$. The backward PQC is the same as in Fig. 10 (b).

- [20] Y. Song, J. Sohl-Dickstein, D. P. Kingma, A. Kumar, S. Ermon, and B. Poole, in *The Ninth International Conference on Learning Representations* (2021).
- [21] A. Schneuing, Y. Du, C. Harris, A. Jamasb, I. Igashov, W. Du, T. Blundell, P. Lió, C. Gomes, M. Welling, M. Bronstein, and B. Correia, *Structure-based drug design with equivariant diffusion models* (2022), arXiv:2210.13695 [q-bio.BM].
- [22] Y. Chen, T. T. Georgiou, and M. Pavon, *Journal of Optimization Theory and Applications* **169**, 671 (2016).
- [23] P. Dhariwal and A. Nichol, *Adv. Neural Inf. Process.* **34**, 8780 (2021).
- [24] G. Müller-Franzes, J. M. Niehues, F. Khader, S. T. Arasteh, C. Haarbinger, C. Kuhl, T. Wang, T. Han, S. Nebelung, J. N. Kather, *et al.*, arXiv preprint arXiv:2212.07501 (2022).
- [25] A. Jalal, M. Arvinte, G. Daras, E. Price, A. G. Dimakis, and J. Tamir, in *Adv. Neural Inf. Process.*, Vol. 34, edited by M. Ranzato, A. Beygelzimer, Y. Dauphin, P. Liang, and J. W. Vaughan (Curran Associates, Inc., 2021) pp. 14938–14954.
- [26] Y. Song and S. Ermon, in *Adv. Neural Inf. Process.*, Vol. 32, edited by H. Wallach, H. Larochelle, A. Beygelzimer, F. d'Alché-Buc, E. Fox, and R. Garnett (Curran Associates, Inc., 2019).
- [27] A. Nahum, J. Ruhman, S. Vijay, and J. Haah, *Phys. Rev. X* **7**, 031016 (2017).
- [28] A. Nahum, S. Vijay, and J. Haah, *Phys. Rev. X* **8**, 021014 (2018).
- [29] R. Harper, S. T. Flammia, and J. J. Wallman, *Nat. Phys.* **16**, 1184 (2020).
- [30] S. Chen, Y. Liu, M. Otten, A. Seif, B. Fefferman, and L. Jiang, *Nat. Commun.* **14**, 52 (2023).
- [31] Q. Zhuang and Z. Zhang, *Phys. Rev. X* **9**, 041023 (2019).
- [32] Y. Xia, W. Li, Q. Zhuang, and Z. Zhang, *Phys. Rev. X* **11**, 021047 (2021).
- [33] J. R. McClean, S. Boixo, V. N. Smelyanskiy, R. Babbush, and H. Neven, *Nat. Commun.* **9**, 4812 (2018).
- [34] M. Cerezo, A. Sone, T. Volkoff, L. Cincio, and P. J. Coles, *Nat. Commun.* **12**, 1791 (2021).
- [35] S. Wang, E. Fontana, M. Cerezo, K. Sharma, A. Sone, L. Cincio, and P. J. Coles, *Nat. Commun.* **12**, 6961 (2021).
- [36] C. Ortiz Marrero, M. Kieferová, and N. Wiebe, *PRX Quantum* **2**, 040316 (2021).
- [37] See Supplementary Information.
- [38] A. Gretton, K. M. Borgwardt, M. J. Rasch, B. Schölkopf, and A. Smola, *J. Mach. Learn. Res.* **13**, 723 (2012).
- [39] C. Villani, *Topics in Optimal Transportation*, Graduate studies in mathematics (American Mathematical Society, 2003).
- [40] O. Oreshkov and J. Calsamiglia, *Phys. Rev. A* **79**, 032336 (2009).
- [41] F. G. Brandao, A. W. Harrow, and M. Horodecki, *Commun. Math. Phys.* **346**, 397 (2016).
- [42] A. W. Harrow and S. Mehraban, *Commun. Math. Phys.* **401** (2023).
- [43] S. Chen, S. Chewi, J. Li, Y. Li, A. Salim, and A. R. Zhang, arXiv:2209.11215 (2022).
- [44] M. C. Caro, H.-Y. Huang, N. Ezzell, J. Gibbs, A. T.

- Sornborger, L. Cincio, P. J. Coles, and Z. Holmes, *Nat. Commun.* **14**, 3751 (2023).
- [45] L. Bianchi, J. Pereira, and S. Pirandola, *PRX Quantum* **2**, 040321 (2021).
- [46] N. Srebro, K. Sridharan, and A. Tewari, *Adv. Neural Inf. Process. Syst.* **23** (2010).
- [47] R. Yao, X. Chen, and Y. Yang, in *Conference on Learning Theory* (PMLR, 2022) pp. 2242–2275.
- [48] R. Belyansky, P. Bienias, Y. A. Kharkov, A. V. Gorshkov, and B. Swingle, *Phys. Rev. Lett.* **125**, 130601 (2020).
- [49] V. Havlíček, A. D. Córcoles, K. Temme, A. W. Harrow, A. Kandala, J. M. Chow, and J. M. Gambetta, *Nature* **567**, 209 (2019).
- [50] M. Schuld, arXiv preprint arXiv:2101.11020 (2021).
- [51] G. Li, R. Ye, X. Zhao, and X. Wang, *Adv. Neural Inf. Process.* **35**, 19456 (2022).
- [52] J. F. Rodriguez-Nieva and M. S. Scheurer, *Nat. Phys.* **15**, 790 (2019).
- [53] X. Chen and Y. Yang, *Appl. Comput. Harmon. Anal.* **52**, 303 (2021).
- [54] R. R. Coifman and S. Lafon, *Appl. Comput. Harmon. Anal.* **21**, 5 (2006), special Issue: Diffusion Maps and Wavelets.
- [55] A. Sornsaeng, N. Dangniam, P. Palittapongarnpim, and T. Chotibut, *Phys. Rev. A* **104**, 052410 (2021).
- [56] A. Skolik, J. R. McClean, M. Mohseni, P. van der Smagt, and M. Leib, *Quantum. Mach.* **3**, 1 (2021).
- [57] E. Campos, D. Rabinovich, V. Akshay, and J. Biamonte, *Phys. Rev. A* **104**, L030401 (2021).
- [58] B. Skinner, J. Ruhman, and A. Nahum, *Phys. Rev. X* **9**, 031009 (2019).
- [59] B. Zhang and Q. Zhuang, *Quantum. Sci. Technol.* **7**, 035017 (2022).
- [60] Y. Song, L. Shen, L. Xing, and S. Ermon, arXiv:2111.08005 (2021).
- [61] T. Hsing and R. Eubank, *Theoretical Foundations of Functional Data Analysis, with an Introduction to Linear Operators*, Wiley Series in Probability and Statistics (Wiley, 2015).
- [62] G. Peyré and M. Cuturi, *Foundations and Trends in Machine Learning* **11**, 355 (2019).
- [63] S. Chakrabarti, H. Yiming, T. Li, S. Feizi, and X. Wu, *Adv. Neural Inf. Process.* **32** (2019).
- [64] G. De Palma, M. Marvian, D. Trevisan, and S. Lloyd, *IEEE Trans. Inf. Theory* **67**, 6627 (2021).
- [65] B. T. Kiani, G. De Palma, M. Marvian, Z.-W. Liu, and S. Lloyd, *Quantum. Sci. Technol.* **7**, 045002 (2022).
- [66] J. A. Smolin and D. P. DiVincenzo, *Phys. Rev. A* **53**, 2855 (1996).
- [67] S.-X. Zhang, J. Allcock, Z.-Q. Wan, S. Liu, J. Sun, H. Yu, X.-H. Yang, J. Qiu, Z. Ye, Y.-Q. Chen, *et al.*, *Quantum* **7**, 912 (2023).
- [68] J. R. Johansson, P. D. Nation, and F. Nori, *Comput. Phys. Commun.* **183**, 1760 (2012).
- [69] R. Flamary, N. Courty, A. Gramfort, M. Z. Alaya, A. Boisbunon, S. Chambon, L. Chapel, A. Corenflos, K. Fatras, N. Fournier, L. Gautheron, N. T. Gayraud, H. Janati, A. Rakotomamonjy, I. Redko, A. Rolet, A. Schutz, V. Seguy, D. J. Sutherland, R. Tavenard, A. Tong, and T. Vayer, *J. Mach. Learn. Res.* **22**, 1 (2021).